Three-dimensional morphology of polymeric membranes from electron tomography

Masoud Ghasemi[1,2], Michael Geitner[1], Agatha O'Connell[2], Enrique D. Gomez[1,2*]

[1] Department of Chemical Engineering, Pennsylvania State University, University Park, PA, 16802, USA

[2] Department of Materials Science and Engineering, Pennsylvania State University, University Park, PA, 16802, USA

[*]To whom correspondence should be addressed. Email: edg12@psu.edu

Abstract

Recent advances in the water-energy landscape hinge upon our improved understanding of the complex morphology of materials involved in water treatment and energy production. Due to their versatility and tunability for applications ranging from drug delivery to fuel cells, polymeric systems will play a crucial role in shaping the future of water-energy nexus applications. Electron tomography stands as a transformative approach for elucidating the intricate structures inherent to polymers, offering unparalleled insights into their nanoscale architectures and functional properties in three dimensions. In particular, the various morphological and chemical characteristics of polymer membranes provide opportunities for perturbations to standard electron tomography for the study of these systems. In this review, we discuss the applications of transmission electron microscopy in establishing structure-function relationships in polymeric membranes with an emphasis on traditional electron tomography (ET) and cryogenic electron tomography (cryo-ET). The synergy between ET and cryo-ET to unravel structural complexities and dynamic behaviors of polymer membranes holds immense potential in driving progress and innovation across frontiers related to water-energy nexus applications.

Introduction

In the rapidly evolving landscape of the water-energy nexus, the interplay between water resources and energy production has emerged as a critical focal point for addressing global sustainability challenges. The efficient utilization of water resources and energy is essential for ensuring environmental preservation(1), economic growth(2), and societal well-being(3). Within this context, the development and optimization of advanced membrane technologies have gained prominence as promising solutions to enhance water treatment, desalination, and energy generation processes. For instance, reverse osmosis (RO) membranes are responsible for over 60% of the global water desalination capacity that is subsequently being used for agriculture, livestock, and energy production(4; 5). As the water-energy nexus continues to shape global sustainability priorities, an urgent need for developing materials characterized by minimal energy consumption for water treatment, and high efficiency in energy production, is being acknowledged by researchers and policy makers around the globe.

Polymeric membranes stand out as a highly promising technology to address challenges in the water-energy nexus(6-8). The successful adaptation of these membranes in applications related to water treatment and energy generation primarily hinges on our enhanced understanding of the microstructures governing their physical and electrical properties(9-11). The morphology of membrane systems can be investigated through different means such as X-ray scattering(12-14), atomic force microscopy(15), and transmission electron microscopy (TEM)(16; 17), to name a few. To this end, scattering techniques (X-ray and Neutron)(18; 19) have been extensively used for the study of phase behavior in polymeric systems. Despite their numerous advantages, scattering methods struggle to reveal key morphological features that are relevant to transport, such as tortuosity, and spatial variation in microstructure and polymer properties. Hence probing the microphase structures and nanodomains of the polymers used in water treatment and energy production applications often relies on the employment of microscopy techniques. However, the utilization of conventional two-dimensional (2D) microscopy and spectroscopy methods rests on the significant presumption that 2D depictions entirely encapsulate the three-dimensional (3D) essence of polymeric membranes and systems.

1. General Principles of Electron Tomography (ET)

1.1. Morphology Characterization in Three Dimensions

The vertical heterogeneity of polymer membranes along the thickness of the film can be imaged by preparing cross-section samples with a focused ion beam (FIB) or microtome(9; 20; 21). In principle, X-ray or neutron reflectivity(22; 23), X-ray photoelectron spectroscopy(24), or time of flight secondary ion mass spectrometry (ToF-SIMS)(25; 26) can also produce depth profiles. Each of these techniques suffers from some limitations; for instance, when using a FIB, structural or chemical damages due to local heating caused by ion beams can alter the micro- and nanostructure of the polymer. Similarly, microtoming, which involves slicing polymer thin sections from bulk samples, can introduce deformations and artifacts in soft samples. Depth profiles provide average information as a function of film thickness but do not reveal the structural details that lead to the average properties. Tomography techniques provide unparalleled insights into the heterogeneity of polymeric membranes and functional materials in 3D. Tomography methods such as X-ray tomography, allow 3D reconstruction of the internal morphology of a specimen through a collection of 2D projections at different tilt angles(27-30). In addition to X-ray tomography, 3D imaging based on transmission electron microscopy techniques has emerged as a pivotal tool in unraveling the intricate structural characteristics of membranes, enabling researchers to design and engineer high-performance membranes for a variety of water-energy nexus applications(31-33). The direct imaging of the structures, high spatial resolution (nm to Å ranges), and the ability to image lightweight elements can be named as some of the main advantages of Electron Tomography (ET) for studying organic and polymeric systems.

1.2. 3D Reconstruction of Organic Specimens

Full 3D reconstruction of a specimen using TEM can be produced using two mian approaches, single particle reconstruction and tomography. Each micrograph from TEM data collection can be regarded as a 2D projection of a 3D object. In single particle analysis, these projections are classified based on their spatial orientation and eventually organized into preferred orientations(34-36). In the next step, through an iterative process, the classified special orientations are used for a more accurate determination of projection angles. To achieve a good final resolution (better than 1 nm) in a reconstructed 3D structure, a large number of individual images (on the order of thousands of images) with an even distribution of identical particles in each image (over 10 particles per image) are usually needed. Hence, the single-particle approach is limited to the specimen with a homogenous distribution of identical particles. In cases such as interfacial science

and polymeric membranes, ET presents the best means to collect 3D information on the specimen. Here, 2D projections of a 3D object are collected as a series of tilt angles, which are then back-projected to reconstruct a 3D model.

1.3. Tilt Series Acquisition

Although the use of ET in material and biological science can be regarded as a gradual progression involving the collective efforts of numerous scientists over several decades, the first employment of the modern ET concept can be dated back to the 1960s(37; 38). As mentioned earlier, ET is based on 2D projections acquired at a series of different tilt angles, making up a "stack." In the next step, the 2D projections are aligned and combined to create a 3D representation of the object (tomogram). The Fourier Slice Theorem is the fundamental mathematical relationship of 3D reconstruction. This theorem connects the two-dimensional Fourier transforms of a 3D object and its corresponding 2D projections. The theorem states that the Fourier transform of a 2D projection at angle θ is equal to the specific slice of the 3D Fourier transform of the initial object at the same angle θ. In practical terms, the Fourier Slice Theorem allows for the reconstruction of a faithful 3D tomogram from its 2D projections by simply taking the inverse Fourier transform of the acquired projections after the generation of aligned stacks. Typically, fiducial markers are used for alignment purposes; these markers are comprised of 5-10 nm gold nanoparticles that are evenly distributed across the sample surface through drop casting, a nebulizer, or dissolving in isopentane-based cryogenic solvents for prolonged low temperature data collection. Fiducial markers allow for the alignment of each image, and automatic image focusing during the data collection(39). On the other hand, manually focusing during image collection, albeit a slower process, can produce higher quality images, especially at higher tilt angles. For further in-depth information on tomography and the algorithms employed for the 3D reconstruction of tilt series, we refer the readers to more comprehensive sources(40-42).

1.4. Resolution

In ET, resolution of final 3D models is often limited by two main factors, restriction of the tilt angles (both in terms of the number of tilt angles and the range, usually between -70° and 70°), and electron radiation damage during extensive data collection at different angles. By considering the *x*-*y* plane as the imaging plane and the *x*-axis as the tilt axis, it can be seen that ET inherently

under-samples the specimen along the *y*-axis due to sample rotation. Hence, assuming a perfect alignment and experimental procedures, the resolution along the *x*-axis is equal to the instrumental resolution acquired in normal 2D images while the resolution along the *y*-axis is further reduced. For a reconstruction of diameter *D* over a full ±90° tilt range, an estimation of the best d_y resolution can be written as $d_y = \pi D/N$, where *N* is the number of equally spaced projections in a tilt series.

The resulting reconstructed tomograms consist of layered brightness-containing pixels to form voxels (3D version of the pixel) with the lowest resolution associated with the projection direction (*z*-axis). The images serve as a map of intensity-per-pixel based on brightness *versus* concentration of electrons transmitted through the sample at a particular pixel. Finally, the voxels are summed to create a larger array containing all sample information needed for reconstruction. The lower resolution along the projection direction is mainly caused by the tilt angle range restriction (usually within ±70°) which causes the formation of a missing wedge (see Fig. 1). This usually leads to an elongation along the projection direction with the elongation factor (e_{yz}) being defined as $d_z = e_{xy}d_y$ where d_z is the best achievable resolution along the *z*-axis. For a tilt range between -70° to +70° the elongation factor is calculated to be ~1.3(43). However, the experimental results show the elongation factor can be smaller than the predicted value with $e_{xy} = 1.1$ reported for ±70° for a rod-shaped sample of zirconia fillers in a polymer matrix(44). The detrimental effect of the missing wedge on resolution along the projection axis can be reduced by performing tomography over two perpendicular axes instead of one, thus reducing the missing wedge to a missing cone/pyramid(45). In addition to the inherent limitations of resolution along the *y*- and *z*-axis, other technical factors such as sample thickness(46; 47), microscope stability, and beam damage can also affect the resolution of the final reconstructed 3D model.

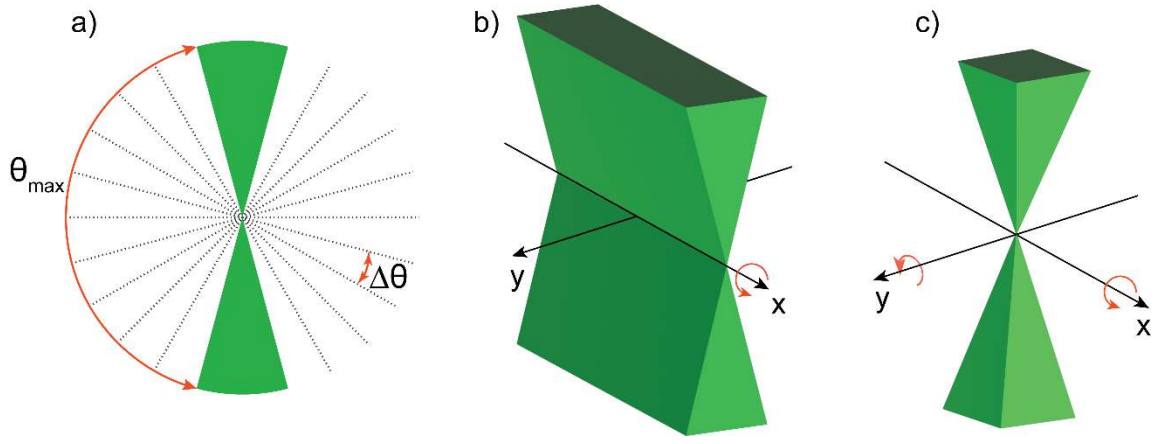

Fig. 1. a) Schematic of tilt series collected at different angles. $\Delta\theta$ angle increment between each subsequent tilt scan. Formation of the missing wedge (b) and missing cone (c) in single and double tilt series data acquisition.

TEM samples should be 100 nm or less to minimize multiple scattering events; often for carbonaceous materials the inelastic scattering cross-section, and not the elastic cross-section, is limiting (48). As the sample is tilted, the section of the sample that the beam must penetrate increases, the need to have the sample at the eucentric height increases substantially, and the probability of inelastic scattering events increases. The path length difference as a function of tilt angle, α, is governed as ~1/cos(α)(49). Furthermore, the holder and the grid can block the beam. Tomography holders are constructed to minimize beam blockage, where the viewing area is designed as ellipsoidal for maximizing the field of view during a tilt series acquisition. Other holders are designed to be used with half-circle grids to minimize interference with imaging.

Various strategies are also being utilized to mitigate radiation damage during the acquisition of tilt series data, with the most effective approach found to be conducting ET measurements at cryogenic temperatures. In cryogenic transmission electron microscopy (cryo-EM), samples are frozen at a cryogenic temperature (below -150 °C). The reduction in specimen temperature first and foremost decreases atomic and molecular diffusion, such that the atomic arrangement, even if damaged, can be preserved. Furthermore, various other aspects may contribute to the reduction of damage, such as the lower rate of inelastic scattering due to the reduced vibrational energy of atoms at low temperatures, and the higher ionization potential of atoms at lower temperatures that reduces the change of ionization damage and secondary degradation events(48). In addition, as we discuss later in this review, cryogenic electron tomography (cryo-ET) also allows the preservation of the hydrated states in polymer membranes, which is crucial for the detailed study of microstructures in these systems in an aqueous environment. To further reduce beam damage during data collection, low-dose data collection with the capability of focusing and tracking on an area close to the area of interest has also been exploited(50).

2. Electron tomography (ET) of Polymeric Systems

2.1. *Electron Tomography of Water Desalination Membranes*

Membranes employed for desalination via reverse osmosis (RO) must be capable of especially high rejection of sodium chloride, with a lower limit of 99.3 percent for single-pass treatment of seawater feeds(51). Commercial RO membranes achieve this separation by employing a dense polymer active layer, typically fully aromatic polyamide, supported by a microporous polysulfone layer and a non-woven polyester backing to provide structural integrity(52; 53). The active layer in these thin-film composite membranes is synthesized directly on top of the polysulfone layer through interfacial polymerization, a rapid reaction between amine and acid-chloride monomers at the interface of immiscible phases (commonly aqueous *m*-phenylenediamine and trimesoyl chloride in hexane)(54; 55). This reaction results in a crosslinked polymer film with a rough surface, internal voids, and inhomogeneous distributions of polymer density and charge(56; 57). Application of electron tomography to the polyamide active layer of RO membranes allows this complex morphology to be resolved in three dimensions, and synthesis-structure-performance relationships to be examined at the nanometer scale.

She et al. demonstrated that ET can be applied to the active layer of a commercial thin-film composite membrane. Their objective was to compare the nanostructure of a polymeric nanofiltration (NF) membrane with that of a model biomimetic filter (specifically a silica-based diatom frustule)(58). NF thin-film composite membranes function similarly to RO thin-film composites, with separation achieved by a dense active layer. The amine monomer in NF interfacial polymerization is typically replaced by piperazine, and the resulting membranes exhibit higher flux but lower sodium chloride rejection(51). The authors prepared NF samples for TEM tomography by applying a thin coating of platinum to the surface of a commercial membrane before milling with a FIB and transferring to a supported TEM grid. Inhomogeneity in the active-layer structure was observed at the nanoscale, indicating the advantage of 3D imaging over two-dimensional methods previously employed. While their work establishes that ET can successfully reconstruct the 3D morphology of the polyamide active layer of a commercial membrane, the authors noted that “major challenges remain” in regard to sample preparation, tomography holder design, and accurate alignment during reconstruction (58).

As part of a study investigating the relationship between active-layer structure and membrane performance, Pacheco et al. utilized ET to compare the structures of brackish water (BW) and seawater (SW) RO membranes, the latter having lower water permeance. The authors isolated the polyamide active layer of thin-film composite membranes by mounting the samples

on TEM grids and then dissolving the polysulfone layer with chloroform, eliminating the potential for sample damage introduced by FIB milling. TEM tomography was performed at 300 kV over ±70 degrees with a Saxton tilt scheme beginning with 2-degree increments, and reconstruction was performed via back-projection; the final resolution of the resulting tomograms was ≤ 5 nm for the *xy*-plane and approximately 10 nm in the *z*-direction. Reconstructions of the BWRO and SWRO membranes both exhibited internal voids that decreased in size approaching the back surfaces of the active layers. However, the authors found that the SWRO membrane showed significantly less void space overall than the BWRO membrane and that voids of similar size to those in the BWRO membrane were enclosed in thicker polyamide when present in the SWRO sample. They suggested that the decreased permeability of their SW sample was due to the increased mass-transfer resistance resulting from these structural differences in its active layer. It was also observed that some voids opened to the back surface of the active layer, while others were completely surrounded by polyamide and closed to both surfaces of the film, revealing more about potential transport pathways in RO membranes(59).

Li et al. performed a study of flow activity in a commercial SWRO membrane by characterizing the deposition of gold nanoparticles of various sizes and charges on the active layer after filtration from either the front or back of the thin-film composite membrane. Two-dimensional imaging of sample cross-sections was performed following filtrations. Briefly, the authors found that the smallest particles (1 nm diameter) filtered from the back side were able to cross the polyamide-polysulfone interface and reach the nodules at the front surface, suggesting that these features have open pathways from the back side of the film. It was also observed that positively charged particles "preferentially aggregate at the surface of the [polyamide] film," indicating that this region has a higher density of carboxyl groups. After front-side filtration of 5-nm particles, aggregates were observed in apparent voids, revealing that these features are actually open to the top surface of the active layer. In order to gain further insight into the polyamide structure, the authors utilized scanning transmission electron microscopy (STEM) tomography to image active-layer samples isolated similarly to those prepared by Pacheco et al. The authors examined the basal layer of the reconstructed active layer separately and observed "discrete voids, of 5-50 nm in diameter" with a total void fraction of approximately 27 percent. At the top surface of the reconstruction, it was determined that many features that appear to be discrete voids in cross-section images are actually open to the outer surface of the active layer, confirming the results of

the front-side nanoparticle filtration experiments. The authors also examined membrane performance in cross-flow filtration at 290 psi over 78 hours and observed an increase in salt rejection from 80 to 98 percent. They contribute this improvement in the rejection to compaction of the membrane, suggesting that compaction may have important impacts on active-layer structure(60).

Culp et al. performed a study focused on the use of ET for the characterization of thin-film composite membrane active layers, comparing the structures of a BWRO and a SWRO membrane. Notably, the membranes were compacted in cross-flow filtration (150 psi for 12 hours) prior to analysis. Active layers were isolated by mounting thin-film composite samples polyamide-side down on a water-soluble, sacrificial layer of polymer coated on a silicon substrate. The polysulfone support was dissolved by organic solvents and the isolated polyamide layer dried before floating and transferring to TEM grids by dissolving the sacrificial layer. The authors demonstrated that the isolation of compacted polyamide films results in minimal changes to the surface morphology compared to virgin membranes via atomic force microscopy, and that "significant morphological changes for hydrated membranes are not expected" for compacted samples by measuring hydrated thicknesses in humidity-controlled ellipsometry. High-angle annular dark-field (HAADF) STEM tomography was utilized; the use of HAADF yields voxel intensities that are directly proportional to sample density, offering further insight into structural inhomogeneities. The reconstructed active layers confirmed previous evidence of apparent voids near the surface being open features contributing to the surface area (see Fig. 2). The total surface area for the 3D reconstructed tomograph of membranes was determined to be approximately twice that measured by atomic force microscopy, which highlights the importance of ET for studying nanostructure of RO membranes. Additionally, closed voids in the compacted active layers were found to account for less than 0.2 percent of the total volume, two orders of magnitude below the values reported for virgin membranes; the authors observe that both membranes contain a void-free region near the bottom of the polyamide layer and suggest that closed voids have little impact on transport overall. Finally, the intensity-density proportionality resulting from HAADF imaging was used to examine local variations in polyamide density. The authors observed that both membranes had inhomogeneous density distributions on the nanoscale. While polyamide density at the "bottom surface is on average of higher density compared with the middle of the film," the highest densities were observed at the top surface, particularly in protruding features. The authors suggest that the

limiting barrier for water permeance is therefore at the top of the active layer, supported by the higher average voxel intensity seen in the SWRO membrane, which has a lower permeability than the BWRO sample(61).

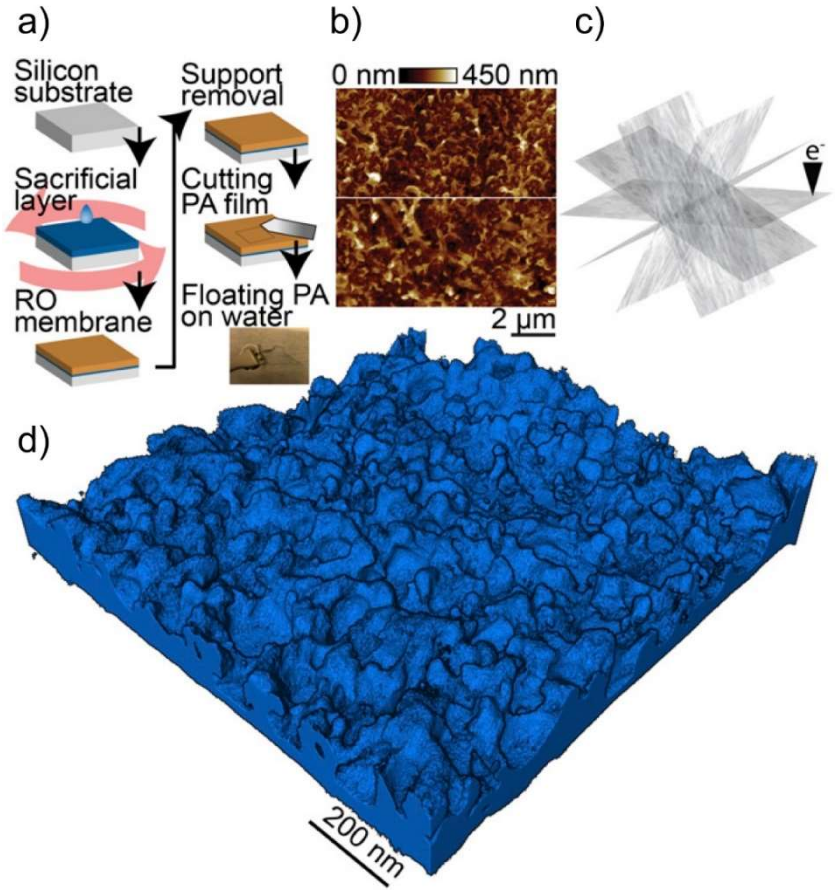

Fig. 2. a) Isolation process of polyamide to be used for ET. b) AFM images of polyamide top surfaces before and after isolation. c) Schematic of ET and tilt series collection. d) Volume rendering image of compressed seawater high-rejection (SWHR) membrane. Reprinted with permission from (62).

In a subsequent study, Culp et al. expanded on this methodology to produce quantifiable polymer densities in reconstructed polyamide active layers and relate density inhomogeneity to membrane performance. The authors performed a multi-modal electron microscopy approach, where HAADF-STEM tomography was done as previously described on a series of four membranes that displayed a counterintuitive increase in water permeability despite increasing active-layer thickness (see Fig. 3), and energy-filtered TEM was used to obtain average properties for the active layers (corroborated by ellipsometry measurements). This enabled the authors to

determine the polyamide density (and therefore water diffusivity) for each voxel in the reconstructed active layers. Water diffusion pathways in the reconstructed active layers were modeled by computationally solving Fick's Law for each voxel. The authors found that the predicted and measured water permeabilities for the four membranes were in good agreement and that the membrane with the highest permeability "[had] the lowest average density and narrowest density distribution." Samples with increased density homogeneity required less lateral diffusion of water within the active layer and therefore exhibited higher permeability despite increasing thickness(63).

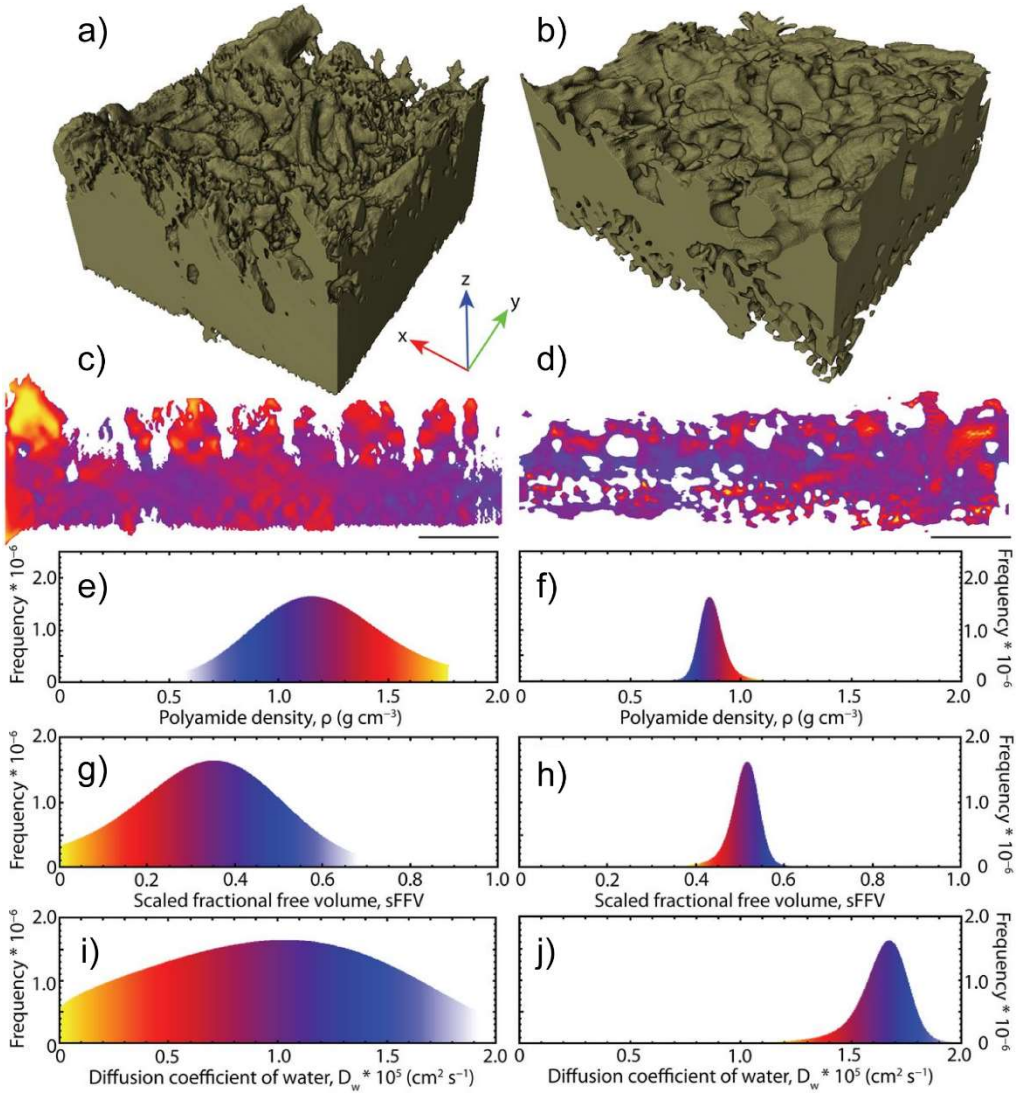

Fig. 3. a) and b) 3D isosurface of two different polyamide membranes PA1 and PA4, respectively. *x-z* plane with colorized voxel of PA1 c), and PA4 d), polymer density e), and f, scaled fractional

free volume, g) and h), and diffusion coefficient of water i), and j) in PA1 and PA4 RO membranes. Scale bars are 200 nm. Reprint with permission from (33).

Further study of the protruding surface features of RO membranes can also clarify structure-performance relationships. Kurihara and Hanakawa used cross-section TEM and ET to image individual protruding features on RO membranes(64). Song et al. "adapted methods from the biological sciences for quantitative morphological analysis" of tomograms of polyamide films. The authors performed interfacial polymerization of *m*-phenylenediamine and trimesoyl chloride on the surface of a polysulfone support coated with a sacrificial layer of cadmium hydroxide nanostrands; the sacrificial layer was etched to float the polyamide film and transfer to a TEM grid. TEM tomography was performed over ±60° in 2-degree increments, and reconstruction was generated via back projection with a final resolution of 0.68 nm. The authors focused on achieving low-dose imaging to prevent altering the polyamide nanostructure during image acquisition. A number of quantitative analyses were performed (see Figure 4 for examples of 3D reconstructed and rendered volume of PA membranes). It was observed that the crumples on the active layer surface significantly increase the surface area relative to the projected area, with the ratio ranging from 3.5 to 15.7 in this study. The structures of individual polyamide crumples were also examined in greater detail. As in previous studies, the authors found that some voids are open to the back surface of the active layer while others are surrounded completely by the polymer. They observed that the active-layer crumples ranged from 4 to 30 percent void by volume within the reconstruction of their synthesized film. Analysis of the local curvature of the crumples was also performed to gain insight into interaction environments for a solute approaching the crumple surface. Based on their findings, the authors divided the polyamide crumples into hollow hemispherical domes, elongated dimples, and clusters that are more convoluted. Further analysis was performed to quantify the local, 3D variation of polyamide thickness within crumple structures. It was determined that "dome crumples have the smallest local thickness, suggesting a shorter permeation pathway for solvent molecules," while dimpled and clustered features have bimodal thickness distributions. Overall, these findings suggest that active layer structure could be the result of uniform pieces of polyamide film collapsing to form more complex structures during the interfacial polymerization process. Crumples of the three classes were also skeletonized, and similar distributions of branch lengths were observed regardless of the overall structure, suggesting

an active-layer feature specific to interfacial polymerization parameters. Finally, the adsorption of metal ions to the polyamide surface was characterized by STEM energy-dispersive X-ray spectroscopy, with lead showing site localization, which is indicative of a structure-performance relationship(65).

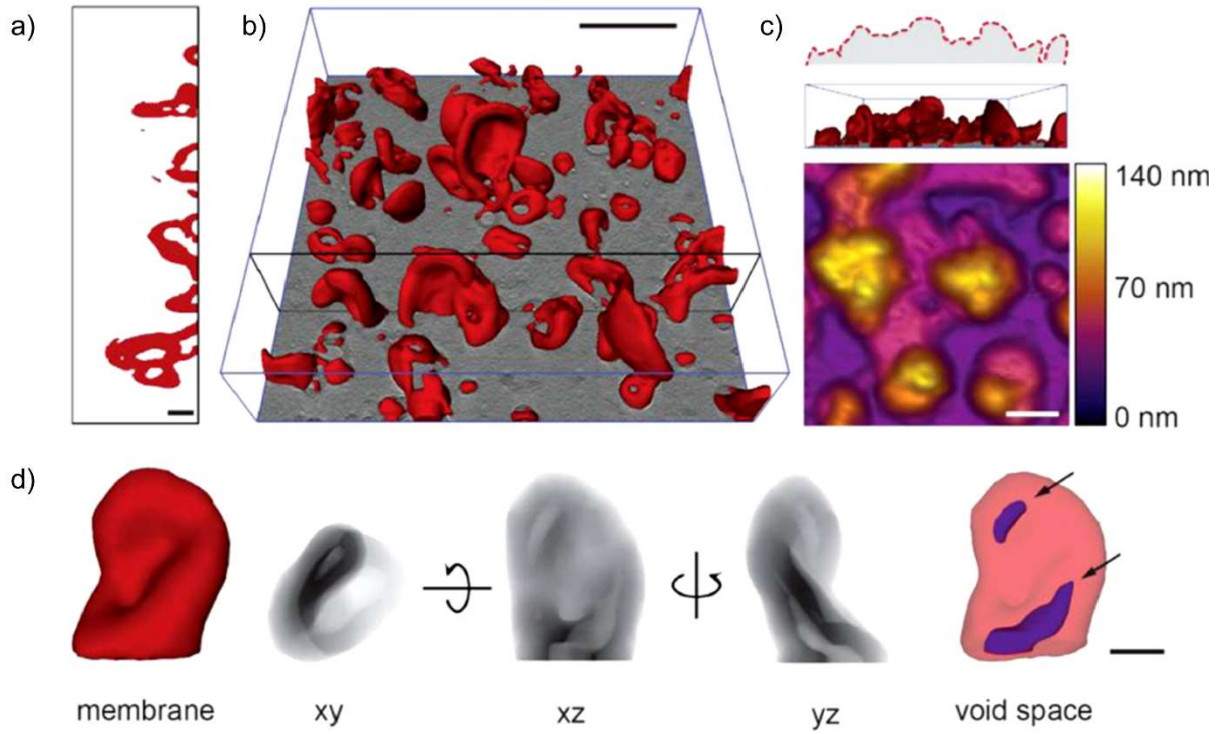

Fig. 4. a) 2D slice of a reconstructed 3D tomogram of PA film. b) 3D tomograph of PA film. c) Side view of reconstructed 3D tomograph and AFM PA film. d) Individual crumples are shown in different orientations, the void spaces are shown in purple. The scale bar corresponds to 200 nm. Adapted with permission from (65). Copyright 2019 American Chemical Society.

An et al. furthered the application of biological morphogenesis to the analysis of thin-film composite active layers at the nanoscale. Examining the effect of varying monomer concentrations on the resulting structures of a series of polyamide films, the authors applied machine learning to classify morphological features and theoretical modeling to predict permeance based on the results of ET. As in their previous study, low-dose ET was utilized to produce reconstructions with 0.68 nm resolution. Polyamide films were synthesized by interfacial polymerization of varying concentrations of aqueous *m*-phenylenediamine (1 to 5 w/v%) and trimesoyl chloride in hexane (0.05 to 1 w/v%). While structural differences resulted from various synthesis conditions, the

authors observed that no differences in morphology remained for reaction times beyond one minute. Both isolated and clustered nodules were observed for the polyamide films, with structures suggesting the simultaneous occurrence of pore formation and nodule protrusion during interfacial polymerization. Furthermore, the pores seen in the reconstructions were resolved as concave areas formed due to the protrusion of a continuous membrane rather than open pores crossing the polyamide film(66).

Analysis of the spatial distribution of these pores was performed, and the authors determined that the characteristic wavelength between neighboring pores directly relates to monomer concentrations during interfacial polymerization. This provides unique quantitative support for the suggestion that the synthesis of these films involves a Turing reaction-diffusion instability. It was also determined that the areal density of pores subsequently impacts the formation of either solo or clustered features in the polyamide. Reconstructions were also used in predicting permeance for the synthesized polyamide films. True surface area, local thickness, and degree of cross-linking (determined from X-ray photoelectron spectroscopy) were used with the Speigler-Kedem model to calculate permeance in good agreement with experimental values. The authors found that differences in membrane structure contribute to 49.3% of the modeled permeance, while the remaining portion can be attributed to variations in material properties, supporting the importance of 3D, morphological characterization in the analysis and understanding of thin-film composite membranes(66).

Finally, An et al. utilized machine learning to categorize crumples through morphometry analysis. Solo crumples were found to belong to three distinct groups (dome, dimple, and pancake). These solo crumple group types and the presence of clusters were consistent across membranes prepared from varying concentrations in interfacial polymerization. The authors demonstrated via liquid-phase atomic force microscopy that the mechanical properties of these features vary between the distinct types. Therefore, they suggest that variation in the distribution of these group types may be used as a tunable parameter (via synthesis) to control the mechanical robustness of polyamide membranes(66). Yao et al. further developed this machine-learning methodology for the analysis of synthesis-nanomorphology relationships in general. Application of their workflow to the polyamide system explored previously identified an additional crumple group type (lay) and allowed the authors to infer that a high trimesoyl chloride concentration could lead to the formation of smaller crumples(67).

Li et al. utilized neural network-assisted image segmentation to improve the segmentation of polymer and vacuum regions in TEM tomograms of thin-film composite polyamide active layers. They were able to significantly reduce the time required for processing of tomogram data. The authors also utilized simplified sample preparation methods and demonstrated reconstruction analysis with results in agreement with previously reported values. They propose an overall workflow from sample preparation to data post-treatment for expedited processing of thin-film composite samples through TEM tomography analysis(68).

2.2. *Electron Tomography of Polymer Electrolytes in a Dry State*

Ionomers are of paramount importance in the transition to a sustainable energy future. The use of ionomers as polymer electrolytes facilitates efficient and low-temperature proton conduction, making polymer electrolyte fuel cells promising candidates for clean and reliable power generation in various applications, including vehicles and portable electronic devices. Nafion as the most widely used ionomer consists of tetrafluoroethylene backbones and hydrophilic perfluoroether side chains with sulfonic acid termini. The morphology and internal structure of Nafion is a matter of great interest for establishing structure-function relationships in this class of ionomers(11). The functionality and operational stability of Nafion-based devices are directly correlated to the distribution of hydrophobic and hydrophilic nanodomains. For instance, the formation of nanoscale ion-depleted regions has been shown to be correlated to the propagation of microcracks in Nafion which in turn leads to mechanical degradation of these systems(69). In addition, Nafion applications extend far beyond polymer electrolyte fuel cells, encompassing biosensing(70; 71), batteries(72; 73), and water electrolysis(74; 75), where films with thicknesses varying from tens of nanometers to micrometers are essential. Thus, understanding Nafion morphology in 3D plays a crucial role in greater control of its properties. Recently, ET has received great attention in the characterization of Nafion nanostructure and phase distribution. This section highlights a few examples of ET applications in the characterization of Nafion ionomers.

Due to low contrast between hydrophilic and hydrophobic phases, high-resolution electron microscopy of Nafion is usually carried out using negative(21), or positive(76), (77) staining methods. In a recent study carried out by Peltonen et al., the 3D morphology of unannealed Nafion was investigated using HAADF-STEM tomography in films with different thicknesses (ranging from 10 to 100 nm)(21). In this study, negative staining with uranyl format (UF) was used to

improve the contrast between hydrophilic and hydrophobic phases. STEM tomography revealed the existence of elongated hydrophilic channels in the dry state of Nafion films, a characteristic typically associated with hydrated Nafion samples. Here, the presence of bicontinuous hydrophilic channels in a dry Nafion specimen was associated with the UF absorption by the hydrophilic channels, which in turn acted as filler and caused partial retention of a hydrated state. Furthermore, STEM tomography of Nafion films with different thicknesses revealed that the volume ratio hydrophilic/hydrophobic is nearly thickness independent. While the hydrophilic channels appeared to be more interconnected (7 nm channel to channel distance) in thicker films, STEM tomography revealed the formation of a higher density of dead-end channels when Nafion films are thicker. STEM tomography results show that the hydrophilic channels had an in-plane preferential orientation, with the exception of 10 nm and 30 nm thick Nafion films, that showed the presence of channels with out-of-plane (*z-axis*) orientation, which had been associated with substrate confinement effects. In summary, exploiting ET allowed the authors to characterize the nanostructure of Nafion thin films in detail, and obtain key information, such as the distribution of hydrophilic phases.

Another important aspect of the 3D morphology of Nafion is the necessity of bicontinuous phases as an ionomer binder in polymer electrolyte fuel cell electrodes(31; 78). These electrodes are composed of carbon black supporting platinum nanoparticles, with Nafion serving as the ionomer binder. To achieve cost proficiency, Pt loading in the cathode electrode needs to remain close to a minimum level (10-20%) without sacrificing polymer electrolyte fuel cell functionalities(79). Nafion's microstructures in polymer electrolyte fuel cell electrodes need to meet three main criteria, i) ensure contact with a maximum number of Pt nanoparticles, ii) maintain connectivity of ionic channels, and iii) allow efficient gas diffusivity through the electrode assembly. To establish the role of Nafion as a binder in electrodes, two sets of samples with different amounts of Nafion in the initial ink were investigated (sample 1, 33 wt%, and sample 2 17 wt%) by Lopez-Haro et al(78). HAADF-STEM tomography was employed to collect tilt series images of carbon black covered Nafion layers. It was revealed that increasing the Nafion composition in the ink did not have a significant effect on the average thickness of the ionomer layer 7.2±2.1 nm versus 7.6±2.2 nm for 33 wt% and 17 wt% samples, respectively. On the other hand, the tomography results showed a clearly different degree of coverage for these samples--amounting to 79.5±2.3% (see Fig. 5) for sample 1, and only 49.9±1.2% for sample 2. The ET

results revealed that the optimal amount of Nafion for full coverage of Pt and carbon black and catalytic performance is 30 wt%, while the connectivity between ionic transport phases could be achieved at lower Nafion composition.

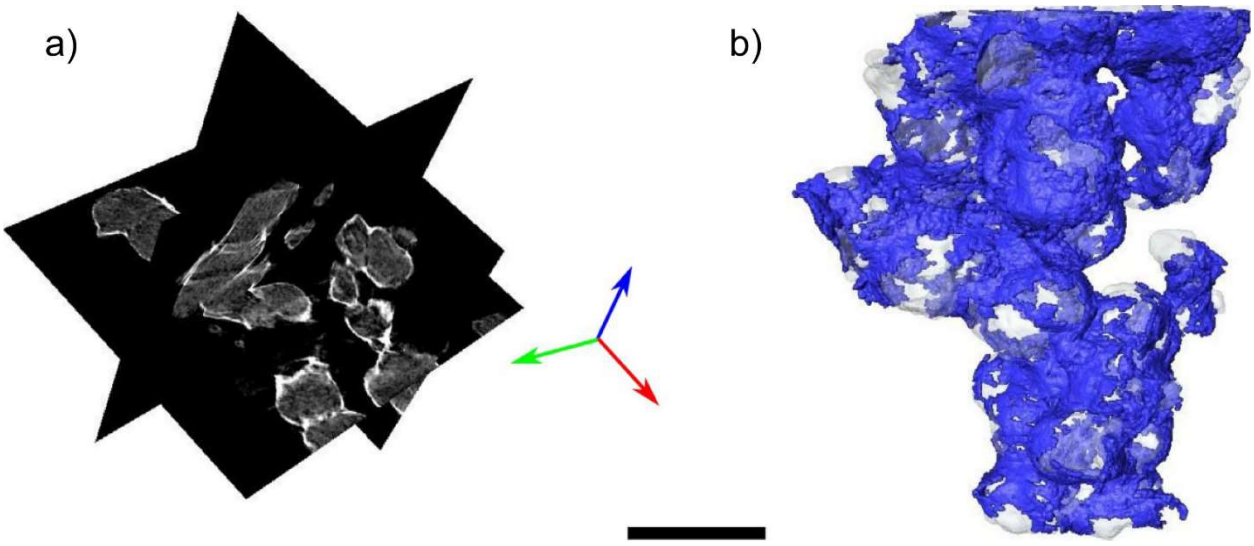

Fig. 5. Orthoslices of sample 1 in imaging plane and projection direction extracted from reconstructed tomograms. 3D reconstructed and rendered volume of sample 1. The blue areas show the stained Nafion ionomers and the transport regions show CB. The scale bar corresponds to 200 nm. Adapted with permission from (78).

2.3. *Electron Tomography Applications in Polymer Solar Cells*

Polymer solar cells hold significant promises in energy conversion and generation technologies(25; 26) due to their lightweight nature, chemical and mechanical flexibility, and adaptability for role-to-role processing. Nanoscale 3D morphology plays a significant role in the performance and stability of polymer solar cells(25; 80). Polymer solar cells generally consist of electron donor and electron acceptor materials mixed in a bulk heterojunction morphology. Nanoscale phase separation and charge percolation pathways can be named as two of the main requirements to achieve highly efficient polymer solar cells. Nanoscale phase separation is required in order to dissociate the photo-generated excitons to free charges. These exciton dissociations take place at the interface of donor/acceptor materials. Due to the limited lifetime and diffusion length of excitons (20-50 nm) a morphology with nanoscale phase separations is

required for efficient exciton dissociation. In the next step, free charge carriers generated at the donor/acceptor interfaces need to be collected at opposite electrodes through percolating pathways to generate a photocurrent. The importance of nanoscale morphology in all three dimensions makes TEM, and ET in particular, ideal tools for morphology characterization(81-83).

Yang et al. carried out the first study exploiting ET to investigate the 3D morphology of polymer:fullerene blends based on poly[2- methoxy-5-(30,70-dimethyloctyloxy)-1,4-phenylene vinylene] (MDMO-PPV) as a donor and the fullerene derivative [6,6]-phenyl-C_{61}-butyric acid methyl ester (PCBM) as an acceptor(84). This study revealed that in MDMO-PPV:PCBM blends, PCBM rich phases are surrounded by MDMO-PPV in all three dimensions. In a follow-up study on the 3D morphology of MDMO-PPV:PCBM, the authors showed that nanoscale PCBM-rich domains are interlinked with PCBM-rich strands, the combination of which formed percolation pathways for dissociated electrons. The use of ET was further extended to other donor:acceptor systems such as poly(3-hexylthiophene) (P3HT):PCBM blends. In particular, the effect of thermal and solvent annealing, as post-processing procedures, on the morphological properties of P3HT:PCBM was characterized using ET. Consistent with former studies(82), in this work 2D TEM micrographs confirmed the formation of P3HT fibers after annealing at elevated temperatures and solvent exposure while the overlapping features of fibers through the thickness of the blends resulted in difficulties in the quantification of fibers' length and distribution. ET revealed the presence of nanoscale networks of both P3HT and PCBM in 3D while such a network could not be detected in as-prepared samples (As shown in Fig. 6). 3D ET also pointed to the enrichment of crystalline P3HT phases close to the bottom interface (hole collecting electrode in conventional geometry). The application of ET to resolve such vertical and lateral heterogeneities is crucial for establishing structure-function relationships in polymer solar cells. Nevertheless, the low electron scattering contrast between the new generation of non-fullerene acceptors and polymer donors could hinder the application of ET in these systems. Recent developments in the field of electron detectors and sample processing techniques, such as staining, create new avenues to investigate the 3D morphology of polymer:non-fullerene blends in nanoscale details using ET (85).

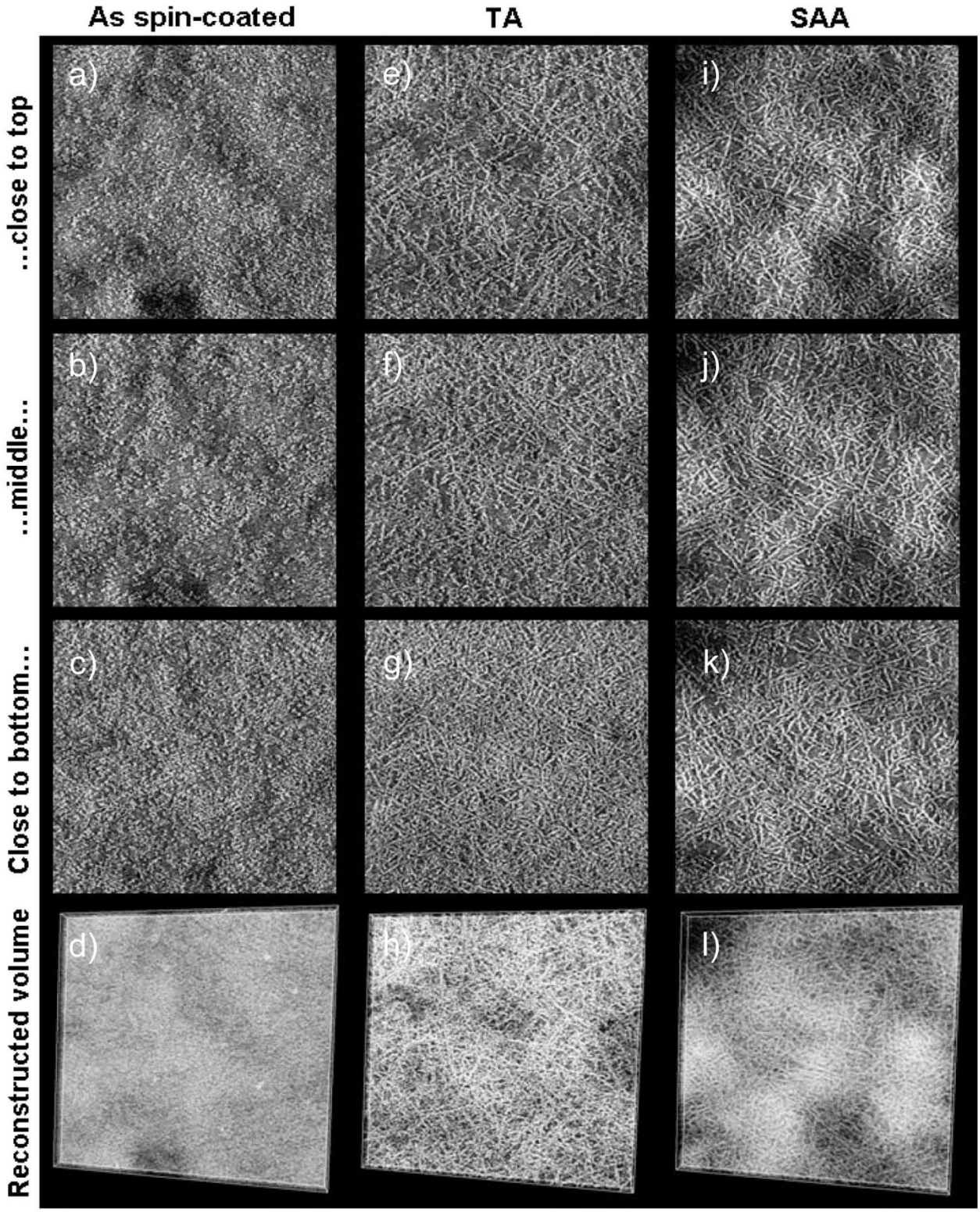

Fig. 6. Aligned TEM micrographs parallel to the electron beam incident axis (imaging plane) at three different positions with respect to the top interface for a) to c) as-prepared samples, e) to g) thermal annealed samples, and i) to k) solvent annealed samples. The reconstructed 3D volume of

d) as prepared, h) thermal annealed, and l) solvent annealed samples. The dimensions of each micrograph are about 1700 nm × 1700 nm. Reprinted with permission from (86). Copyright 2009 American Chemical Society.

3. Cryogenic electron tomography (cryo-ET)

As mentioned before, radiation damage is one of the main factors limiting the resolution of reconstructed tomograms of polymeric systems. In addition, establishing structure-function relationships in systems such as polymers electrolytes, and biomolecules(87) requires preserving the hydrated or aqueous state of these systems. Subsequently, cryo-EM has been rapidly becoming an attractive technique for the characterization of organic systems. For example, cryo-EM combined with tomography capabilities creates a unique opportunity for studying polymeric membranes in the hydrated state(88-90). Although cryogenic electron tomography (cryo-ET) has the potential to improve the resolution of reconstructed tomographs, phenomena such as buckling of the ice layer can lead to beam-induced motion in the microscope(36; 91). This further emphasizes the importance of auto-tracking and auto-focus functions during the acquisition of the tilt series.

Plunge freezing is the standard and most widely used method for the preparation of hydrated cryo-EM samples. This method was first developed by Dubochet et al. in the 1980s to suppress the formation of ice crystals in vitrified thin aqueous films(92; 93). In this method, excess amount of solution (usually water) is removed by blotting the TEM grids using filter paper. Subsequently, the blotted grid is plunged into liquid ethane as the coolant liquid. In the cases of organic solvents, generally liquid nitrogen is used as the coolant liquid due to the solubility of organic solvents' ice in liquid ethane or propane(94; 95). Over the years more methods of sample preparation for sample vitrification have been developed by researchers, which can be categorized as droplet-based and scribing-based methods in addition to the traditional blotting method(96) (as shown in Fig. 7). In droplet-based techniques, millimeter sized droplets are formed which subsequently land on the TEM grid. Due to the elimination of the blotting step in this method, vitrified samples can be prepared at a higher rate compared to the blotting method. On the other hand, in the scribing-based method, a sample is hovered over a TEM grid without directly touching the grid. As a result, a thin layer of liquid fills the holes on TEM grids. The presence of shear force

in the coating of the material makes this method also amenable to the coating process used for the preparation of organic thin films.

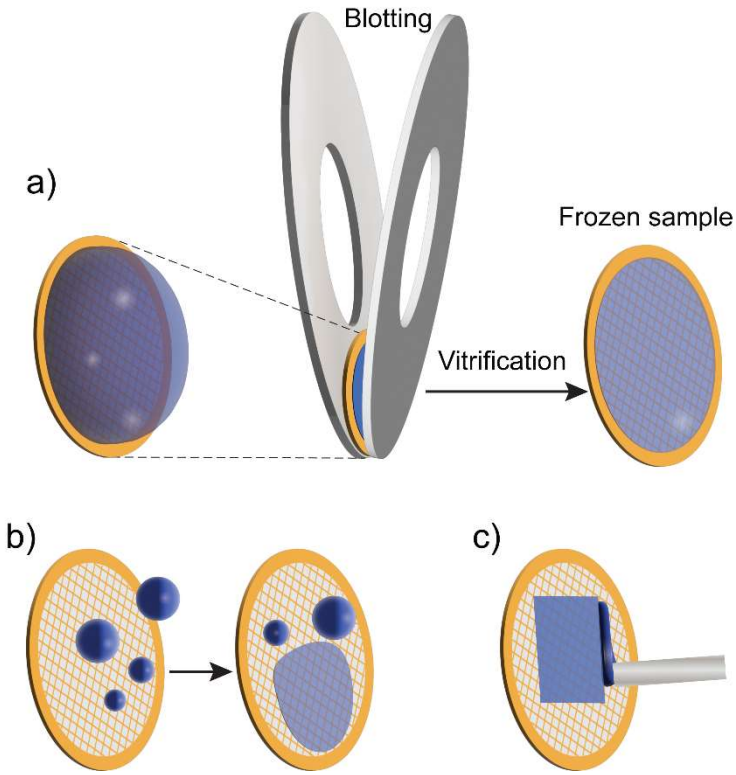

Fig. 7. Schematics of a) blotting, b) droplet, and c) scribing-based techniques for vitrification and preparation of cryo-EM samples.

Although the unique advantages of cryo-ET had been discovered and known in the field of biological science(46; 97; 98), its applications for synthetic materials remained mainly unexplored until the last decade. In 2008 Parry et al. presented the first example of cryo-ET use for the investigation of the internal structure of amphiphilic double-comb block copolymer with hydrophobic leucinyl-valinyl-leucine methyl ester (LVL) and hydrophilic oligo ethylene glycol (OEG) side chains(99). In this work, cryo-ET provided compelling evidence, revealing an internal structure characterized by a bicontinuous network of branched peptide-containing worm-like micelles. The presence of such bicontinuous nanostructures intertwined with the hydrated channels in an aggregate dispersion would be hard to observe using conventional X-ray scattering techniques, if at all possible. The authors further show that the aggregation behavior of the

hydrated double-comb block copolymer used in this study was directed by the specific amino acid sequence of the peptide graft rather than by the hydrophilic–hydrophobic balance of the polymers.

Since then, the unparalleled advantage of cryo-ET in resolving internal nano- and microstructures of polymer aggregate dispersions has been exploited by different groups. McKenzie et al.(100) showed a temperature-dependent behavior of bicontinuous microstructures formed in poly(ethylene oxide)-block-poly(octadecyl methacrylate) (PEO_{39}-*b*-$PODMA_{17}$). Cryo-ET revealed a bicontinuous PODMA-rich network intertwined with hydrated PEO channels, for the solutions vitrified at 4 °C (Figure 8)**.** Cryo-ET further revealed that vitrification of the aggregate solution kept at a higher temperature (45 °C) leads to the loss of the complex bicontinuous phase. The lack of microstructures in higher-temperature processed samples was associated with the melting of the octadecyl chains in the aggregates (T_{trans} = 21.8 °C). Here the use of cryo-ET provided the capability to capture the temperature-responsive morphology of block copolymers. In general, the variety of complex microstructures and aggregates, captured by cryo-EM and cryo-ET, such as micelles, vesicles, and platelets formed during the self-assembly of amphiphilic block copolymers in dilute solutions show that these structures can be achieved through manipulation of block copolymers chemical structures and change in physical condition of the systems(101; 102).

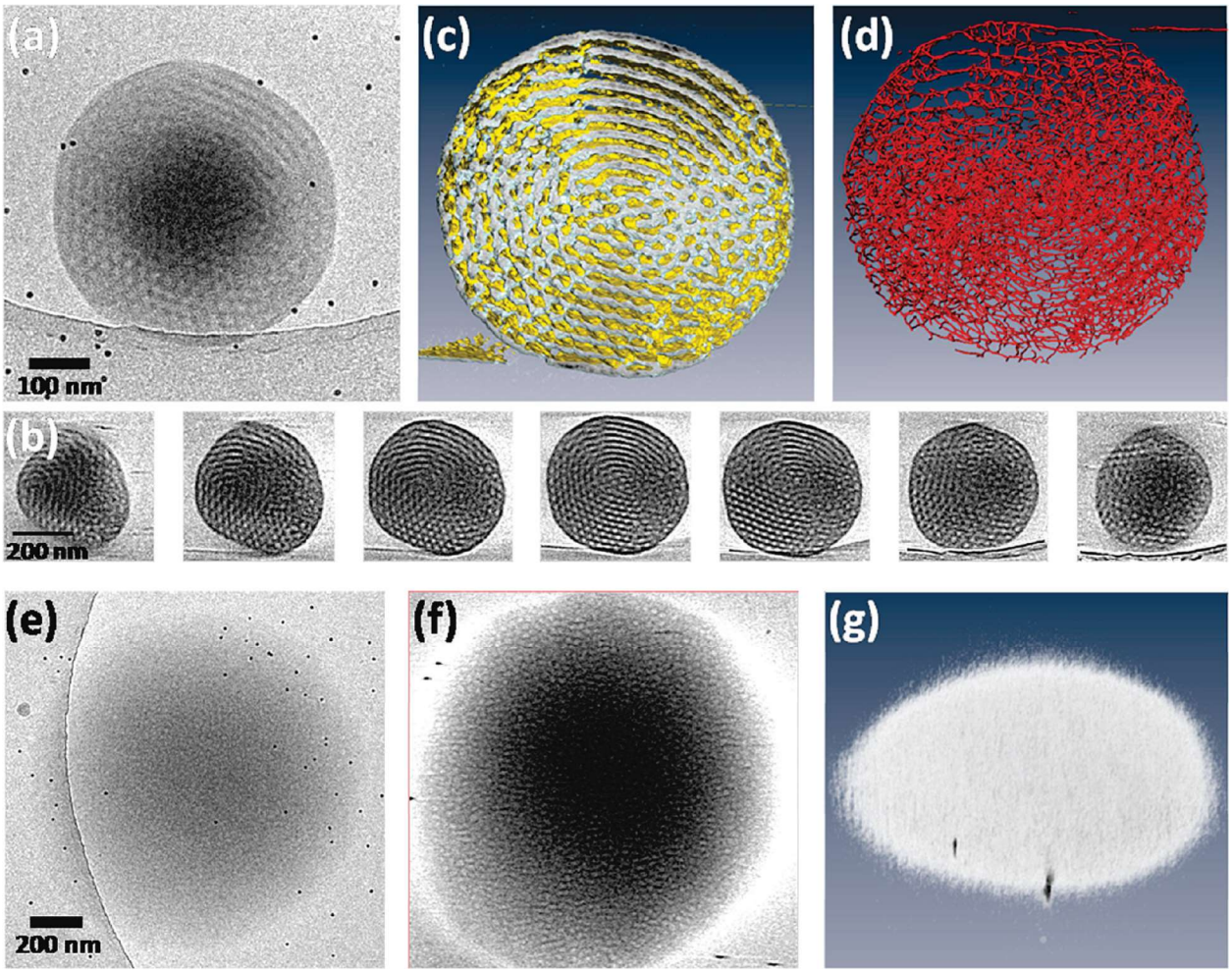

Fig. 8. a) Cryo-EM 2D micrograph of PEO_{39}-*b*-$PODMA_{17}$ micelles vitrified at 4 °C. b) Different tilt images of PEO_{39}-*b*-$PODMA_{17}$ in *x*-*y* plane extracted from aligned the 3D tomogram of PEO_{39}-*b*-$PODMA_{17}$. 3D Reconstructed structure of PEO_{39}-*b*-$PODMA_{17}$ showing the bicontinuous structure in which the yellow surface shows the surface in contact with water channels. d) skeletonization of c). e) Cryo-EM 2D micrograph of PEO_{39}-*b*-$PODMA_{17}$ micelles vitrified at 45 °C. f) *x*-*y* plane slice of the reconstructed tomogram at e). g) volume rendering structure of PEO_{39}-*b*-$PODMA_{17}$ vitrified at 45 °C. Reprinted with permission from (100). Copyright 2010 American Chemical Society.

In recent years, polymer electrolytes have been receiving considerable attention due to their applications in fuel cells(103; 104), redox flow cells(105; 106), batteries(10; 107), and organic electrochemical transistors(108-110). These applications in general rely on the ionic conductivity of the constituent polymer electrolytes. Due to the limited chain motion, sequestration of ionic

clusters, and the lack of ionic percolation pathways, many polymer electrolytes act as ionic insulators in a dry state(111). Hence, the presence of solvents such as water plays a crucial role in ionic transport, and functionality, of polymer electrolyte-based devices(112; 113). Not surprisingly, cryo-ET has also been gaining traction in studies of polymer electrolytes in hydrated states due to its capability to capture visual images of internal microphases and nanodomains.

The formation of microphase-separated hydrated channels is vital for efficient proton conduction in polymer electrolytes(6; 114). In an extensive study, Chen et al. investigated the effects of hydration on nanodomains swelling of sulfonated polystyrene-*b*-polyethylene-*b*-polystyrene (S-SES) triblock copolymers with varying amounts of sulfonation(115). A series of S-SES triblock copolymers with different amounts of homopolymer polystyrene (hPS) were prepared to investigate the effect of morphology on the swelling behavior of the nanodomains. STEM micrographs of dry films show that the samples with a low volume fraction of hPS (<40 vol%) exhibited a lamellar morphology while further addition of hPS to SES caused a transition from lamellar to bicontinuous morphology. Hydrated samples also exhibited lamellar and bicontinuous morphologies similar to their dry film counterparts. The hydrated lamellar samples showed the formation of hydrophobic polyethylene, PSS-rich, and water-rich channels. While the formation of the water-rich channels could not be observed in triblock copolymer S-SES with bicontinuous morphology. Cryo-ET further revealed a significant swelling of the PSS-rich phases while maintaining the bicontinuous morphology in these samples.

In a study conducted by Xi et al., well-defined hydrated vesicles were demonstrated in a series of phosphonate polypeptoid diblock copolymers, namely poly-N-(2-ethyl)hexylglycine-block-poly-N-phosphonomethylglycine (pNeh-*b*-pNpm), with varying chain lengths(116). Compared to sulfonated block copolymers, phosphonate block copolymers exhibited efficient proton conductivity with a lower degree of hydration. As a result, in this study, the authors adopted a water vapor annealed method for cryo-ET sample preparation as opposed to the fully hydrated block copolymers formed by direct contact with water drops.

Cryo-ET of hydrated $pNeh_9$-*b*-$pNpm_9$ (Fig. 9) revealed the presence of dark bands representing the vesicle walls, indicating the coexistence of hydrophobic and hydrophilic blocks within the copolymer. Interestingly, cryo-ET not only unveiled unilamellar and multilamellar vesicles but also uncovered a multi-compartment structure, where larger vesicles enclosed smaller ones. Moreover, the chain length was found to significantly influence the morphology and internal

structures of the vesicles in pNeh-*b*-pNpm systems. Specifically, pNeh$_9$-*b*-pNpm$_9$ absorbed more water, leading to the formation of larger, loosely packed vesicles, whereas pNeh$_{18}$-*b*-pNpm$_{18}$ (longer chains) showed hydration resulting in smaller, more closely packed vesicles. The complex chain-length-dependent hydration and drying mechanisms of vesicles underscore the importance of cryo-ET in revealing these unique morphologies.

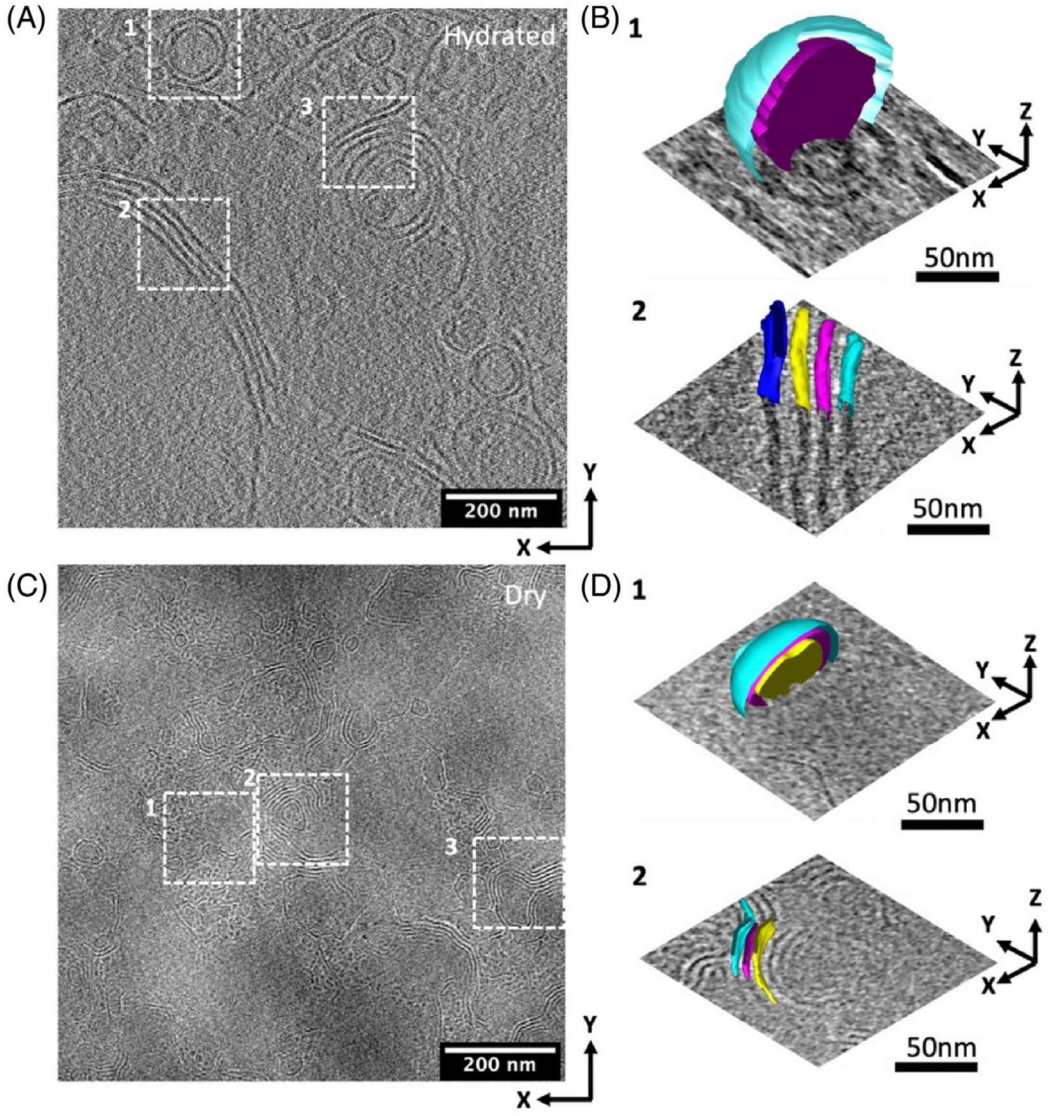

Fig. 9: Tomogram slices of hydrated and dry pNeh$_9$-*b*-pNpm$_9$ samples a) and c), respectively. b) and d) 3D visualization of tomograms from regions of interest shown in (a) and (c) achieved through mesh rendering of the reconstructed tomographs. Reprinted, by permission, from (116). Copyright 2021 John Wiley & Sons, Inc.

Similar to other polymer electrolytes, the structure-property relation of Nafion in polymer electrolyte fuel cells is closely governed by the microstructure of hydrophobic phases and connectivity of the hydrophilic ionic nanochannels hydrated states. Electron microscopy revealed the existence of isolated sulfonic-acid-containing phases in dry Nafion membranes. In contrast, cryo-EM of hydrated Nafion membranes showed the formation of interconnected hydrophilic nanochannels with ~5 nm domain spacing(117) which is consistent with the high ionic conductivity of hydrated Nafion(113). In addition, the operational stability of polymer electrolyte fuel cells is closely correlated to the ability of the polymer ionomers to maintain their initial microstructures(69; 118). By employing cryo-ET, Venkatesan et al. showed that mechanical/chemical degradation of Nafion membranes in a hydrated state causes a reduction in the volume fraction of hydrophilic ionic cluster which in turn leads to the formation of locally depleted and isolated ionic domains(77). These studies showcase the versatile capabilities of cryo-ET in investigating micro- and nanostructures in the field of physical science.

Summary

ET has provided unique opportunities for understanding the 3D structure of polymer membranes. Through these detailed understandings, important functional properties such as water diffusion in polymer membranes could directly be linked to the nanoscale structure of these polymers. In addition, cryo-ET has emerged as an important tool for analyzing polymer microstructures either to reduce the beam damage or to preserve the microstructures in a solvated state. Nevertheless, due to the later adaptation of cryo-ET in synthetic soft matter science compared to the field of structural biology, the full potential of this technique has yet to be explored. As ET and cryo-ET technologies continue to evolve, we envision leveraging these techniques to delve into finer structural details, capturing transient phenomena, and new applications such as bioelectronics applications based on mixed ionic electronic polymers. Additionally, the advancement of data processing algorithms will facilitate the extraction of quantitative information from complex tomographic datasets, enabling the creation of predictive models for membrane behavior and performance.

References

1. Schnoor JL. 2011. Water–Energy Nexus. *Environmental Science & Technology* 45:5065-
2. Lee S-H, Taniguchi M, Masuhara N, Mohtar RH, Yoo S-H, Haraguchi M. 2021. Analysis of industrial water–energy–labor nexus zones for economic and resource-based impact assessment. *Resources, Conservation and Recycling* 169:105483
3. Morales-García M, Rubio MÁG. 2023. Sustainability of an economy from the water-energy-food nexus perspective. *Environment, Development and Sustainability*
4. Caldera U, Breyer C. 2017. Learning Curve for Seawater Reverse Osmosis Desalination Plants: Capital Cost Trend of the Past, Present, and Future. *Water Resources Research* 53:10523-38
5. Fritzmann C, Löwenberg J, Wintgens T, Melin T. 2007. State-of-the-art reverse osmosis desalination. *Desalination* 216:1-76
6. Jr. DTH, Balsara NP. 2013. Polymer Electrolytes. *Annual Review of Materials Research* 43:503-25
7. Geise GM, Lee H-S, Miller DJ, Freeman BD, McGrath JE, Paul DR. 2010. Water purification by membranes: The role of polymer science. *Journal of Polymer Science Part B: Polymer Physics* 48:1685-718
8. Bassyouni M, Abdel-Aziz MH, Zoromba MS, Abdel-Hamid SMS, Drioli E. 2019. A review of polymeric nanocomposite membranes for water purification. *Journal of Industrial and Engineering Chemistry* 73:19-46
9. Russell KP, Zydney AL, Gomez ED. 2023. Impact of virus filter pore size / morphology on virus retention behavior. *Journal of Membrane Science* 670:121335
10. Yuan R, Teran AA, Gurevitch I, Mullin SA, Wanakule NS, Balsara NP. 2013. Ionic Conductivity of Low Molecular Weight Block Copolymer Electrolytes. *Macromolecules* 46:914-21
11. Gierke TD, Munn GE, Wilson FC. 1981. The morphology in nafion perfluorinated membrane products, as determined by wide- and small-angle x-ray studies. *Journal of Polymer Science: Polymer Physics Edition* 19:1687-704
12. Paddison SJ. 2003. Proton Conduction Mechanisms at Low Degrees of Hydration in Sulfonic Acid–Based Polymer Electrolyte Membranes. *Annual Review of Materials Research* 33:289-319
13. Rivnay J, Inal S, Salleo A, Owens RM, Berggren M, Malliaras GG. 2018. Organic electrochemical transistors. *Nature Reviews Materials* 3:17086
14. Rivnay J, Inal S, Collins BA, Sessolo M, Stavrinidou E, et al. 2016. Structural control of mixed ionic and electronic transport in conducting polymers. *Nature Communications* 7:11287
15. Magonov SN, Reneker DH. 1997. CHARACTERIZATION OF POLYMER SURFACES WITH ATOMIC FORCE MICROSCOPY. *Annual Review of Materials Science* 27:175-222
16. Jinnai H, Jiang X. 2013. Electron tomography in soft materials. *Current Opinion in Solid State and Materials Science* 17:135-42
17. Yakovlev S, Balsara NP, Downing KH. 2013. Insights on the Study of Nafion Nanoscale Morphology by Transmission Electron Microscopy. *Membranes* 3:424-39
18. Chan EP, Frieberg BR, Ito K, Tarver J, Tyagi M, et al. 2020. Insights into the Water Transport Mechanism in Polymeric Membranes from Neutron Scattering. *Macromolecules* 53:1443-50
19. Heller WT. 2022. Small-Angle Neutron Scattering for Studying Lipid Bilayer Membranes. *Biomolecules* 12:1591
20. Li Y, Kłosowski MM, McGilvery CM, Porter AE, Livingston AG, Cabral JT. 2017. Probing flow activity in polyamide layer of reverse osmosis membrane with nanoparticle tracers. *Journal of Membrane Science* 534:9-17
21. Peltonen A, Etula J, Seitsonen J, Engelhardt P, Laurila T. 2021. Three-Dimensional Fine Structure of Nanometer-Scale Nafion Thin Films. *ACS Applied Polymer Materials* 3:1078-86
22. Singh MA, Groves MN. 2009. Depth profiling of polymer films with grazing-incidence small-angle X-ray scattering. *Acta Crystallogr A* 65:190-201
23. Rus ED, Dura JA. 2019. In Situ Neutron Reflectometry Study of Solid Electrolyte Interface (SEI) Formation on Tungsten Thin-Film Electrodes. *ACS Appl Mater Interfaces* 11:47553-63

24. Heilmann A, Werner J, Kelly M, Holloway B, Kay E. 1997. XPS depth profiles and optical properties of plasma polymer multilayers with embedded metal particles. *Applied Surface Science* 115:365-76
25. Ghasemi M, Balar N, Peng Z, Hu H, Qin Y, et al. 2021. A molecular interaction–diffusion framework for predicting organic solar cell stability. *Nature Materials* 20:525-32
26. Ghasemi M, Ye L, Zhang Q, Yan L, Kim J-H, et al. 2017. Panchromatic Sequentially Cast Ternary Polymer Solar Cells. *Adv. Mater.* 29:1604603
27. Withers PJ, Bouman C, Carmignato S, Cnudde V, Grimaldi D, et al. 2021. X-ray computed tomography. *Nature Reviews Methods Primers* 1:18
28. Krüger P, Markötter H, Haußmann J, Klages M, Arlt T, et al. 2011. Synchrotron X-ray tomography for investigations of water distribution in polymer electrolyte membrane fuel cells. *Journal of Power Sources* 196:5250-5
29. Viguié J, Savart T, Duru P, Rouch JC, Remigy JC. 2013. Characterisation of 3D porous macrostructure of hollow fibre membranes using X-ray tomography—Effects of some spinning process conditions. *Journal of Membrane Science* 435:11-20
30. Lee S-H, Chang W-S, Han S-M, Kim D-H, Kim J-K. 2017. Synchrotron X-ray nanotomography and three-dimensional nanoscale imaging analysis of pore structure-function in nanoporous polymeric membranes. *Journal of Membrane Science* 535:28-34
31. Uchida H, Song JM, Suzuki S, Nakazawa E, Baba N, Watanabe M. 2006. Electron Tomography of Nafion Ionomer Coated on Pt/Carbon Black in High Utilization Electrode for PEFCs. *The Journal of Physical Chemistry B* 110:13319-21
32. An H, Smith JW, Ji B, Cotty S, Zhou S, et al. 2022. Mechanism and performance relevance of nanomorphogenesis in polyamide films revealed by quantitative 3D imaging and machine learning. *Science Advances* 8:eabk1888
33. Culp TE, Khara B, Brickey KP, Geitner M, Zimudzi TJ, et al. 2021. Nanoscale control of internal inhomogeneity enhances water transport in desalination membranes. *Science* 371:72-5
34. Wu M, Lander GC, Herzik MA. 2020. Sub-2 Angstrom resolution structure determination using single-particle cryo-EM at 200 keV. *Journal of Structural Biology: X* 4:100020
35. Fan X, Wang J, Zhang X, Yang Z, Zhang J-C, et al. 2019. Single particle cryo-EM reconstruction of 52 kDa streptavidin at 3.2 Angstrom resolution. *Nature Communications* 10:2386
36. Naydenova K, Jia P, Russo CJ. 2020. Cryo-EM with sub–1 Å specimen movement. *Science* 370:223-6
37. Hart RG. 1968. Electron Microscopy of Unstained Biological Material: The Polytropic Montage. *Science* 159:1464-7
38. De Rosier DJ, Klug A. 1968. Reconstruction of Three Dimensional Structures from Electron Micrographs. *Nature* 217:130-4
39. Gruska M, Medalia O, Baumeister W, Leis A. 2008. Electron tomography of vitreous sections from cultured mammalian cells. *Journal of Structural Biology* 161:384-92
40. Chen M, Bell JM, Shi X, Sun SY, Wang Z, Ludtke SJ. 2019. A complete data processing workflow for cryo-ET and subtomogram averaging. *Nature Methods* 16:1161-8
41. Tang G, Peng L, Baldwin PR, Mann DS, Jiang W, et al. 2007. EMAN2: An extensible image processing suite for electron microscopy. *Journal of Structural Biology* 157:38-46
42. Ercius P, Alaidi O, Rames MJ, Ren G. 2015. Electron Tomography: A Three-Dimensional Analytic Tool for Hard and Soft Materials Research. *Adv Mater* 27:5638-63
43. Radermacher M. 1988. Three-dimensional reconstruction of single particles from random and nonrandom tilt series. *J Electron Microsc Tech* 9:359-94
44. Kawase N, Kato M, Nishioka H, Jinnai H. 2007. Transmission electron microtomography without the "missing wedge" for quantitative structural analysis. *Ultramicroscopy* 107:8-15
45. Sugimori H, Nishi T, Jinnai H. 2005. Dual-Axis Electron Tomography for Three-Dimensional Observations of Polymeric Nanostructures. *Macromolecules* 38:10226-33

46. Koster AJ, Grimm R, Typke D, Hegerl R, Stoschek A, et al. 1997. Perspectives of Molecular and Cellular Electron Tomography. *Journal of Structural Biology* 120:276-308
47. DIEBOLDER CA, KOSTER AJ, KONING RI. 2012. Pushing the resolution limits in cryo electron tomography of biological structures. *Journal of Microscopy* 248:1-5
48. Williams DB, Carter CB, Williams DB, Carter CB. 1996. *The transmission electron microscope*. Springer
49. Gan L, Jensen GJ. 2012. Electron tomography of cells. *Quarterly Reviews of Biophysics* 45:27-56
50. Dierksen K, Typke D, Hegerl R, Koster AJ, Baumeister W. 1992. Towards automatic electron tomography. *Ultramicroscopy* 40:71-87
51. Baker RW. 2012. Reverse Osmosis. In *Membrane Technology and Applications*:207-51. United Kingdom: John Wiley & Sons Ltd. Number of 207-51 pp.
52. Kah Peng Lee TCA, Davide Mattia. 2011. A review of reverse osmosis membrane materials for desalination-Development to date and future potential. *Journal of Membrane Science* 370:1-22
53. W.J. Lau AFI, N. Misdan, M.A. Kassim. 2012. A recent progress in thin film composite membrane: A review. *Desalination* 287:190-9
54. Baker RW. 2012. Membranes and Modules. In *Membrane Technology and Applications*:207-51. United Kingdom: John Wiley & Sons Ltd. Number of 207-51 pp.
55. Paul W. Morgan SLK. 1959. Interfacial Polycondensation. II. Fundamentals of Polymer Formation at Liquid Interfaces. *Journal of Polymer Science: Part A: Polymer Chemistry* 34:531-59
56. R.J. Peterson JEC. 1990. Thin Film Composite Reverse Osmosis Membranes. In *Handbook of Industrial Membrane Technology*, ed. MC Porter:307-48. New Jersey: Noyes Publications. Number of 307-48 pp.
57. Freger V. 2003. Nanoscale Heterogeneity of Polyamide Membranes Formed by Interfacial Polymerization. *Langmuir* 19:4791-7
58. F.H. She KN, W.M. Gao, P.D. Hodgson, H. Jinnai, L.X. Kong. 2010. 3-Dimensional characterization of membrane with nanoporous structure using TEM tomography and image analysis. *Desalination* 250:757-61
59. Federico Pacheco RS, Martin Reinhard, James O. Leckie, Ingo Pinnau. 2016. 3D visualization of the internal nanostructure of polyamide thin films in RO membranes. *Journal of Membrane Science* 501:33-44
60. Yuqiong Li MMK, Catriona M. McGilvery, Alexandra E. Porter, Andrew G. Livingston, João T. Cabral. 2017. Probing flow activity in polyamide layer of reverse osmosis membrane with nanoparticle tracers. *Journal of Membrane Science* 534:9-17
61. Tyler E. Culp Y-xS, Michael Geitner, Mou Paul, Abhishek Roy, Michael J. Behr, Steve Rosenberg, Junsi Gu, Manish Kumar, Enrique D. Gomez. 2018. Electron tomography reveals details of the internal microstructure of desalination membranes. *Proceedings of the National Academy of Sciences* 115:8694-9
62. Culp TE, Shen Y-x, Geitner M, Paul M, Roy A, et al. 2018. Electron tomography reveals details of the internal microstructure of desalination membranes. *Proceedings of the National Academy of Sciences* 115:8694-9
63. Tyler E. Culp BK, Kaitlyn P. Brickey, Michael Geitner, Tawanda J. Zimudzi, Jeffrey D. Wilbur, Steven D. Jons, Abhishek Roy, Mou Paul, Baskar Ganapathysubramanian, Andrew L. Zydney, Manish Kumar, Enrique D. Gomez. 2021. Nanoscale control of internal inhomogeneity enhances water transport in desalination membranes. *Science* 371:72-5
64. Masaru Kurihara MH. 2013. Mega-ton Water System: Japanese national research and development project on seawater desalination and wastewater reclamation. *Desalination* 308:131-7
65. Xiaohui Song JWS, Juyeong Kim, Nestor J. Zaluzec, Wenxiang Chen, Hyosung An, Jordan M. Dennison, David G. Cahill, Matthew A Kulzick, Qian Chen. 2019. Unraveling the Morphology-Function Relationships of Polyamide Membranes Using Quantitative Electron Tomography. *ACS Applied Materials & Interfaces* 11:8517-26

66. Hyosung An JWS, Bingqiang Ji, Stephen Cotty, Shan Zhou, Lehan Yao, Falon C. Kalutantirige, Wenxiang Chen, Zihao Ou, Xiao Su, Qian Chen. 2022. Mechanism and performance relevance of nanomorphogenesis in polyamide films revealed by quantitative 3D imaging and machine learning. *Science Advances* 8:eabk1888
67. Lehan Yao HA, Shan Zhou, Ahyoung Kim, Erik Luijten, Qian Chen. 2022. Seeking regularity from irregularity: unveiling the synthesis-nanomorphology relationships of heterogeneous nanomaterials using unsupervised machine learning. *Nanoscale* 14:16497-89
68. Danyang Li RL, Kunpeng Wang, Yanjie Li, Weichen Lin, Xiao-mao Wang, Yue-xiao Shen, Xia Huang. 2023. Neural Network-Assisted Data Processing Improved Tomography Characterizations of Reverse Osmosis Polyamide Layers. *ACS ES&T Engineering* XXXX:XXX-XXX
69. Venkatesan Sv, Lim C, Holdcroft S, Kjeang E. 2016. Progression in the Morphology of Fuel Cell Membranes upon Conjoint Chemical and Mechanical Degradation. *Journal of The Electrochemical Society* 163:F637
70. Plekhanova Y, Tarasov S, Reshetilov A. 2021. Use of PEDOT:PSS/Graphene/Nafion Composite in Biosensors Based on Acetic Acid Bacteria. *Biosensors* 11:332
71. Lu J, Drzal LT, Worden RM, Lee I. 2007. Simple Fabrication of a Highly Sensitive Glucose Biosensor Using Enzymes Immobilized in Exfoliated Graphite Nanoplatelets Nafion Membrane. *Chemistry of Materials* 19:6240-6
72. Yu X, Joseph J, Manthiram A. 2015. Polymer lithium–sulfur batteries with a Nafion membrane and an advanced sulfur electrode. *Journal of Materials Chemistry A* 3:15683-91
73. Liang HY, Qiu XP, Zhang SC, Zhu WT, Chen LQ. 2004. Study of lithiated Nafion ionomer for lithium batteries. *Journal of Applied Electrochemistry* 34:1211-4
74. Siracusano S, Baglio V, Nicotera I, Mazzapioda L, Aricò AS, et al. 2017. Sulfated titania as additive in Nafion membranes for water electrolysis applications. *International Journal of Hydrogen Energy* 42:27851-8
75. Ito H, Maeda T, Nakano A, Takenaka H. 2011. Properties of Nafion membranes under PEM water electrolysis conditions. *International Journal of Hydrogen Energy* 36:10527-40
76. Xue T, Trent JS, Osseo-Asare K. 1989. Characterization of nafion® membranes by transmission electron microscopy. *Journal of Membrane Science* 45:261-71
77. Venkatesan SV, El Hannach M, Holdcroft S, Kjeang E. 2017. Probing nanoscale membrane degradation in fuel cells through electron tomography. *Journal of Membrane Science* 539:138-43
78. Lopez-Haro M, Guétaz L, Printemps T, Morin A, Escribano S, et al. 2014. Three-dimensional analysis of Nafion layers in fuel cell electrodes. *Nature Communications* 5:5229
79. Lee M, Uchida M, Yano H, Tryk DA, Uchida H, Watanabe M. 2010. New evaluation method for the effectiveness of platinum/carbon electrocatalysts under operating conditions. *Electrochimica Acta* 55:8504-12
80. Ghasemi M, Hu H, Peng Z, Rech JJ, Angunawela I, et al. 2019. Delineation of Thermodynamic and Kinetic Factors that Control Stability in Non-Fullerene Organic Solar Cells. *Joule* 3:1328-48
81. Kuei B, Kabius B, Gray JL, Gomez ED. 2018. Strategies for elemental mapping from energy-filtered TEM of polymeric materials. *MRS Communications* 8:1321-7
82. Kozub DR, Vakhshouri K, Orme LM, Wang C, Hexemer A, Gomez ED. 2011. Polymer Crystallization of Partially Miscible Polythiophene/Fullerene Mixtures Controls Morphology. *Macromolecules* 44:5722-6
83. Köntges W, Perkhun P, Kammerer J, Alkarsifi R, Würfel U, et al. 2020. Visualizing morphological principles for efficient photocurrent generation in organic non-fullerene acceptor blends. *Energy & Environmental Science* 13:1259-68
84. Yang X, Loos J. 2007. Toward High-Performance Polymer Solar Cells: The Importance of Morphology Control. *Macromolecules* 40:1353-62
85. Kuei B, Aplan MP, Litofsky JH, Gomez ED. 2020. New opportunities in transmission electron microscopy of polymers. *Materials Science and Engineering: R: Reports* 139:100516

86. Bavel SSv, Sourty E, With Gd, Loos J. 2009. Three-Dimensional Nanoscale Organization of Bulk Heterojunction Polymer Solar Cells. *Nano Letters* 9:507-13
87. Barcena M, Oostergetel G, Bartelink W, Faas GGA, Verkleij A, et al. 2009. Cryo-electron tomography of mouse hepatitis virus: Insights into the structure of the coronavirion. *Proceedings of the National Academy of Sciences* 106:582-7
88. Mkenzie BE, Holder SJ, Sommerdijk NAJM. 2012. Assessing internal structure of polymer assemblies from 2D to 3D CryoTEM: Bicontinuous micelles. *Current Opinion in Colloid & Interface Science* 17:343-9
89. Patterson JP, Xu Y, Moradi M-A, Sommerdijk NAJM, Friedrich H. 2017. CryoTEM as an Advanced Analytical Tool for Materials Chemists. *Accounts of Chemical Research* 50:1495-501
90. Newcomb CJ, Moyer TJ, Lee SS, Stupp SI. 2012. Advances in cryogenic transmission electron microscopy for the characterization of dynamic self-assembling nanostructures. *Current Opinion in Colloid & Interface Science* 17:350-9
91. Jiang X, Xuan S, Zuckermann RN, Glaeser RM, Downing KH, Balsara NP. 2021. Minimizing Crinkling of Soft Specimens Using Holey Gold Films on Molybdenum Grids for Cryogenic Electron Microscopy. *Microscopy and Microanalysis* 27:767-75
92. Dubochet J, Adrian M, Chang J-J, Homo J-C, Lepault J, et al. 1988. Cryo-electron microscopy of vitrified specimens. *Quarterly Reviews of Biophysics* 21:129-228
93. Dubochet J, McDowall AW. 1981. VITRIFICATION OF PURE WATER FOR ELECTRON MICROSCOPY. *Journal of Microscopy* 124:3-4
94. Matatyaho Ya'akobi A, Talmon Y. 2021. Extending Cryo-EM to Nonaqueous Liquid Systems. *Accounts of Chemical Research* 54:2100-9
95. Oostergetel GT, Esselink FJ, Hadziioannou G. 1995. Cryo-Electron Microscopy of Block Copolymers in an Organic Solvent. *Langmuir* 11:3721-4
96. Weissenberger G, Henderikx RJM, Peters PJ. 2021. Understanding the invisible hands of sample preparation for cryo-EM. *Nature Methods* 18:463-71
97. Auer M. 2000. Three-dimensional electron cryo-microscopy as a powerful structural tool in molecular medicine. *Journal of Molecular Medicine* 78:191-202
98. Dierksen K, Typke D, Hegerl R, Walz J, Sackmann E, Baumeister W. 1995. Three-dimensional structure of lipid vesicles embedded in vitreous ice and investigated by automated electron tomography. *Biophysical Journal* 68:1416-22
99. Parry AL, Bomans PHH, Holder SJ, Sommerdijk NAJM, Biagini SCG. 2008. Cryo Electron Tomography Reveals Confined Complex Morphologies of Tripeptide-Containing Amphiphilic Double-Comb Diblock Copolymers. *Angewandte Chemie International Edition* 47:8859-62
100. McKenzie BE, Nudelman F, Bomans PHH, Holder SJ, Sommerdijk NAJM. 2010. Temperature-Responsive Nanospheres with Bicontinuous Internal Structures from a Semicrystalline Amphiphilic Block Copolymer. *Journal of the American Chemical Society* 132:10256-9
101. Yu H, Jiang W. 2009. Effect of Shear Flow on the Formation of Ring-Shaped ABA Amphiphilic Triblock Copolymer Micelles. *Macromolecules* 42:3399-404
102. Gomez ED, Rappl TJ, Agarwal V, Bose A, Schmutz M, et al. 2005. Platelet Self-Assembly of an Amphiphilic A−B−C−A Tetrablock Copolymer in Pure Water. *Macromolecules* 38:3567-70
103. Meier-Haack J, Taeger A, Vogel C, Schlenstedt K, Lenk W, Lehmann D. 2005. Membranes from sulfonated block copolymers for use in fuel cells. *Separation and Purification Technology* 41:207-20
104. Elabd YA, Hickner MA. 2011. Block Copolymers for Fuel Cells. *Macromolecules* 44:1-11
105. Liu QH, Grim GM, Papandrew AB, Turhan A, Zawodzinski TA, Mench MM. 2012. High Performance Vanadium Redox Flow Batteries with Optimized Electrode Configuration and Membrane Selection. *Journal of The Electrochemical Society* 159:A1246
106. Chalamala BR, Soundappan T, Fisher GR, Anstey MR, Viswanathan VV, Perry ML. 2014. Redox Flow Batteries: An Engineering Perspective. *Proceedings of the IEEE* 102:976-99

107. Bouchet R, Maria S, Meziane R, Aboulaich A, Lienafa L, et al. 2013. Single-ion BAB triblock copolymers as highly efficient electrolytes for lithium-metal batteries. *Nature Materials* 12:452-7
108. Tropp J, Meli D, Rivnay J. 2023. Organic mixed conductors for electrochemical transistors. *Matter* 6:3132-64
109. Lyu D, Jin Y, Magusin PCMM, Sturniolo S, Zhao EW, et al. 2023. Operando NMR electrochemical gating studies of ion dynamics in PEDOT:PSS. *Nature Materials*
110. Harikesh PC, Yang C-Y, Wu H-Y, Zhang S, Donahue MJ, et al. 2023. Ion-tunable antiambipolarity in mixed ion–electron conducting polymers enables biorealistic organic electrochemical neurons. *Nature Materials* 22:242-8
111. Paulsen BD, Fabiano S, Rivnay J. 2021. Mixed Ionic-Electronic Transport in Polymers. *Annual Review of Materials Research* 51:73-99
112. Zawodzinski TA, Davey J, Valerio J, Gottesfeld S. 1995. The water content dependence of electro-osmotic drag in proton-conducting polymer electrolytes. *Electrochimica Acta* 40:297-302
113. Choi P, Jalani NH, Datta R. 2005. Thermodynamics and Proton Transport in Nafion: II. Proton Diffusion Mechanisms and Conductivity. *Journal of The Electrochemical Society* 152:E123
114. Chen XC, Wong DT, Yakovlev S, Beers KM, Downing KH, Balsara NP. 2014. Effect of Morphology of Nanoscale Hydrated Channels on Proton Conductivity in Block Copolymer Electrolyte Membranes. *Nano Letters* 14:4058-64
115. Chen XC, Jiang X, Balsara NP. 2018. Swelling of individual nanodomains in hydrated block copolymer electrolyte membranes. *The Journal of Chemical Physics* 149:163325
116. Jiang X, Sun J, Zuckermann RN, Balsara NP. 2021. Effect of hydration on morphology of thin phosphonate block copolymer electrolyte membranes studied by electron tomography. *Polymer Engineering & Science* 61:1104-15
117. Allen FI, Comolli LR, Kusoglu A, Modestino MA, Minor AM, Weber AZ. 2015. Morphology of Hydrated As-Cast Nafion Revealed through Cryo Electron Tomography. *ACS Macro Letters* 4:1-5
118. Lim C, Ghassemzadeh L, Van Hove F, Lauritzen M, Kolodziej J, et al. 2014. Membrane degradation during combined chemical and mechanical accelerated stress testing of polymer electrolyte fuel cells. *Journal of Power Sources* 257:102-10